

# Perturbation equations for all-scale atmospheric dynamics

Piotr K. Smolarkiewicz<sup>a</sup>, Christian Kühnlein<sup>a</sup>, Nils P. Wedi<sup>a</sup>

<sup>a</sup>*European Centre For Medium-Range Weather Forecasts, Reading, RG2 9AX, UK*

---

## Abstract

This paper presents generalised perturbation forms of the nonhydrostatic partial differential equations (PDEs) that govern dynamics of all-scale global atmospheric flows. There can be many alternative perturbation forms for any given system of the governing PDEs, depending on the assumed ambient state about which perturbations are taken and on subject preferences in the numerical model design. All such forms are mathematically equivalent, yet they have different implications for the design and accuracy of effective semi-implicit numerical integrators of the governing PDEs. Practical and relevant arguments are presented in favour of perturbation forms based on the solutions' computational efficacy. The optional forms are implemented in the high-performance finite-volume module (IFS-FVM) for simulating global all-scale atmospheric flows [Smolarkiewicz et al., *J. Comput. Phys.* (2016) doi:10.1016/j.jcp.2016.03.015]. The implementation of the general and flexible perturbation formulation is illustrated and verified with a class of ambient states of reduced complexity. A series of numerical simulations of the planetary baroclinic instability, epitomising global weather, illustrates the accuracy of the perturbation equations. The novel numerical approach has the potential for numerically accurate separation of a background state from finite-amplitude perturbations of the global atmosphere. Practical implications include far less sensitivity to grid imprinting on non-uniform meshes, undiluted interaction of background shear with rotational motions, and an improved accuracy and reliability of extended-range predictions.

*Key words:* atmospheric models, flexible PDEs, nonoscillatory forward-in-time schemes, numerical weather prediction, climate

*PACS:*

---

\* Corresponding Author.

*Email address:* smolar@ecmwf.int (Piotr K. Smolarkiewicz).

# 1 INTRODUCTION

An important characteristic of the atmospheric dynamics is that it constitutes a relatively small perturbation about dominant hydrostatic and geostrophic balances established in effect of the Earth gravity, rotation, stably-stratified thermal structure of its atmosphere and the energy provided by the incoming flux of solar radiation. For illustration, consider that the total conversion of available potential energy to kinetic energy in the global atmosphere is only 0.26% of the incoming solar radiation at the top of the atmosphere; cf. Fig. 1 in [46]. Preserving this fundamental equilibrium, while accurately resolving the perturbations about it, conditions the design of atmospheric models and subjects their numerical procedures to intricate stability and accuracy requirements. In particular, extended-range (11-45 days) and seasonal weather predictions (up to 1 year ahead) are subjected to dominant initial and model biases in the simulation of the atmosphere/ocean and suffer from low signal-to-noise ratios. In seasonal forecasting, this proves a difficult problem for the detection of anomalies, especially when there is also a model drift relative to long-term biases in the simulated quantities [20]. The conceptual idea of the approach implemented in this paper is a numerically accurate separation and dual evolution of an arbitrary (but advantageously selected) ambient state and finite-amplitude perturbations around this state, to improve conservation properties, mean state bias and drift, and the reliability of extended-range predictions.

Given the nature of atmospheric dynamics, it is compelling to formulate governing PDEs in terms of perturbation variables about an arbitrary state of the atmosphere that already satisfies some or all of the dominant balances. In fact, this is a standard approach in small-scale atmospheric modelling based on soundproof equations, such as the classical incompressible Boussinesq system or its anelastic or pseudo-incompressible generalisations. The key role of the reference state in these equation systems is to uncouple a dominating hydrostatic balance from buoyancy driven motions, and to justify linearisations required to achieve a physically-relevant complexity reduction. Otherwise, the reference state does not have to be unique nor represent the actual mean state of the system. The primary strength of established reference states is their generally recognized theoretical and practical validity. However, such reference states are overly limited, most often consisting only of a single stably or neutrally stratified vertical profile of thermodynamic variables. To alleviate this limitation, soundproof models often account for an additional, more general balanced state, hereafter referred to as an “ambient” state [27].

The notion of ambient states is distinct from that of the reference state. The utilization of an ambient state is justified by expediency and optional for any system of the governing equations. The role of ambient states is to enhance the

efficacy of numerical simulation—e.g. by simplifying the design of the initial and boundary conditions and/or improving the conditioning of elliptic boundary value problems—without resorting to linearisation of the system. The key underlying assumption is that the ambient state is a particular solution of the governing problem, so that subtracting its own minimal set of PDEs from the governing equations can provide a useful perturbation form of the governing system. In general, ambient states are not limited to stable or neutral stratifications [8], can be spatially and temporally varying to represent, e.g. thermally balanced large-scale steady flows in atmospheric models [26,35] or prescribe oceanic tidal motions [39]. Here, we present a generalised formalism allowing, in principle, for an arbitrary (yet advantageous) ambient state. In the context of this development, it is hoped that there are special cases of such arbitrary states that can be particularly useful for weather and climate applications. All theoretical developments directly pertain to two advanced all-scale modelling systems, the Eulerian-Lagrangian (EULAG) research model for multi-scale flows [23,34,35] and the Finite-Volume Module (IFS-FVM) [36,13,37] in the Integrated Forecasting System (IFS) of the European Centre for Medium-Range Weather Forecasts (ECMWF).

The paper is organised as follows: Section 2 derives the perturbation form of the nonhydrostatic compressible Euler equations of all-scale atmospheric dynamics. The related numerical procedures are described in Section 3. Section 4 substantiates technical developments of the preceding sections, with a series of simulations of the planetary baroclinic instability. Section 5 concludes the paper.

## 2 GOVERNING EQUATIONS

### 2.1 *Generic form*

The generalised PDEs of EULAG [35] and IFS-FVM [36] assume the compressible Euler equations under gravity on a rotating sphere as default, but include reduced soundproof equations [18,6] as options. From the perspective of numerics, the design of the semi-implicit integrators in FVM follows the same path for the compressible and the anelastic system. Hence, we focus on the most general case of the compressible Euler equations. For simplicity, we start the presentation with the physically more intuitive advective form of the inviscid governing equations formulated on a rotating sphere, and introduce the corresponding conservation forms implemented in FVM afterwards in Section 3. With these caveats, the advective forms of equations for density  $\rho$ , potential temperature  $\theta$  and the physical velocity vector  $\mathbf{u}$  can be compactly

written as

$$\frac{d\rho}{dt} = -\frac{\rho}{\mathcal{G}}\nabla \cdot (\mathcal{G}\mathbf{v}) , \quad (1a)$$

$$\frac{d\theta}{dt} = \mathcal{H} , \quad (1b)$$

$$\frac{d\mathbf{u}}{dt} = -\frac{\theta}{\theta_0}\widetilde{\mathbf{G}}\nabla\phi + \mathbf{g} - \mathbf{f} \times \mathbf{u} + \mathbf{M}(\mathbf{u}) + \mathbf{D}(\mathbf{u}) . \quad (1c)$$

Here,  $d/dt = \partial/\partial t + \mathbf{v} \cdot \nabla$ , with  $\nabla = (\partial_x, \partial_y, \partial_z)$  representing a vector of spatial partial derivatives with respect to the generalised curvilinear coordinates  $\mathbf{x} = (x, y, z)$  [22,42,11] (assumed stationary for the purpose of this paper) and  $\mathbf{v} = \widetilde{\mathbf{G}}^T \mathbf{u}$ , where  $\widetilde{\mathbf{G}}$  denotes a  $3 \times 3$  matrix of known metric coefficients. Furthermore,  $\mathcal{G}$  symbolises the Jacobian—i.e. the square root of the determinant of the metric tensor—whereas  $\mathbf{f}$  and  $\mathbf{M}(\mathbf{u})$  respectively mark the vectors of Coriolis parameter and metric forcings (i.e., Christoffel terms) shown for a plain geospherical framework in Appendix A. In (1b),  $\mathcal{H}$  symbolises a heat source/sink, including diffusion. In (1c),  $\mathbf{g}$  is the vector of gravitational acceleration, while  $\mathbf{D}(\mathbf{u})$  symbolises momentum dissipation. The pressure variable  $\phi = c_p\theta_0\pi$  renormalises the Exner-function of pressure,  $\pi := (p/p_0)^{R/c_p} = T/\theta$ , upon which it satisfies the gas law

$$\phi = c_p\theta_0 \left[ \left( \frac{R}{p_0} \rho\theta \right)^{R/c_v} \right] . \quad (2)$$

Here,  $c_p$  and  $c_v$  denote specific heats at constant pressure and volume, respectively,  $R$  is a gas constant,  $T$  indicates the temperature, and subscripts “0” refer to constant reference values.

## 2.2 Ambient state

We now assume an arbitrary ambient state  $(\rho_a, \theta_a, \phi_a, \mathbf{u}_a)$  that satisfies the same generic form of the governing equations, or a subset thereof,

$$\frac{d_a\rho_a}{dt} = -\frac{\rho_a}{\mathcal{G}}\nabla \cdot \mathcal{G}\mathbf{v}_a , \quad (3a)$$

$$\frac{d_a\theta_a}{dt} = \mathcal{H}_a , \quad (3b)$$

$$\frac{d_a\mathbf{u}_a}{dt} = -\frac{\theta_a}{\theta_0}\widetilde{\mathbf{G}}\nabla\phi_a + \mathbf{g} - \mathbf{f} \times \mathbf{u}_a + \mathbf{M}(\mathbf{u}_a) + \mathbf{D}(\mathbf{u}_a) , \quad (3c)$$

where  $d_a/dt = \partial/\partial t + \mathbf{v}_a \cdot \nabla$  with  $\mathbf{v}_a = \widetilde{\mathbf{G}}^T \mathbf{u}_a$ . Correspondingly, the ambient pressure variable  $\phi_a = c_p \theta_0 \pi_a$  satisfies

$$\phi_a = c_p \theta_0 \left[ \left( \frac{R}{p_0} \rho_a \theta_a \right)^{R/c_v} \right], \quad (4)$$

### 2.3 Perturbation forms

#### 2.3.1 Derivation

In order to derive perturbation forms of the governing equations (1b) and (1c), the perturbation dependent variables are first defined as

$$\theta' := \theta - \theta_a, \quad \mathbf{u}' := \mathbf{u} - \mathbf{u}_a, \quad \phi' := \phi - \phi_a. \quad (5)$$

Second, the two auxiliary relations are derived:

$$\forall \psi = \psi' + \psi_a, \quad \frac{d\psi}{dt} - \frac{d_a \psi_a}{dt} \equiv \frac{d\psi'}{dt} + \mathbf{v}' \cdot \nabla \psi_a; \quad (6a)$$

$$\frac{\theta}{\theta_0} \widetilde{\mathbf{G}} \nabla \phi - \frac{\theta_a}{\theta_0} \widetilde{\mathbf{G}} \nabla \phi_a \equiv \frac{\theta}{\theta_0} \widetilde{\mathbf{G}} \nabla \phi' + \frac{\theta'}{\theta_0} \widetilde{\mathbf{G}} \nabla \phi_a. \quad (6b)$$

Then subtracting (3b) from (1b) and (3c) from (1c), and rearranging the terms while using (6a) and (6b), leads to the perturbation forms

$$\frac{d\theta'}{dt} = -\mathbf{v}' \cdot \nabla \theta_a + \mathcal{H}', \quad (7a)$$

$$\begin{aligned} \frac{d\mathbf{u}'}{dt} = & -\mathbf{v}' \cdot \nabla \mathbf{u}_a - \frac{\theta}{\theta_0} \widetilde{\mathbf{G}} \nabla \phi' - \frac{\theta'}{\theta_0} \widetilde{\mathbf{G}} \nabla \phi_a \\ & - \mathbf{f} \times \mathbf{u}' + \mathcal{M}'(\mathbf{u}', \mathbf{u}_a) + \mathcal{D}'(\mathbf{u}', \mathbf{u}_a), \end{aligned} \quad (7b)$$

where

$$\begin{aligned} \mathcal{H}' &= \mathcal{H} - \mathcal{H}_a, \\ \mathbf{v}' &= \widetilde{\mathbf{G}}^T \mathbf{u}', \\ \mathcal{M}'(\mathbf{u}', \mathbf{u}_a) &= \mathcal{M}(\mathbf{u}' + \mathbf{u}_a) - \mathcal{M}(\mathbf{u}_a), \\ \mathcal{D}'(\mathbf{u}', \mathbf{u}_a) &= \mathcal{D}(\mathbf{u}' + \mathbf{u}_a) - \mathcal{D}(\mathbf{u}_a), \end{aligned} \quad (8)$$

the last of which reduces to  $\mathcal{D}' = \mathcal{D}(\mathbf{u}')$  for a solution-independent viscosity.

Among the two perturbation equations in (7), the entropy equation (7a) is straightforward to interpret. The corresponding (specific) momentum equation (7b) is revealing, in that it reduces a total of all ambient forcings into a

generalised 3D buoyancy term relating to  $\theta' \nabla \phi_a$  on the rhs. This can be seen readily when representing  $\widetilde{\mathbf{G}} \nabla \phi_a$  in terms of (3c) as

$$\widetilde{\mathbf{G}} \nabla \phi_a = \frac{\theta_0}{\theta_a} \left( \mathbf{g} - \mathbf{f} \times \mathbf{u}_a + \mathbf{M}(\mathbf{u}_a) + \mathbf{D}(\mathbf{u}_a) - \frac{d_a \mathbf{u}_a}{dt} \right). \quad (9)$$

Importantly, substituting (9) in (7b) and manipulating the terms—such as to separate the gravitational, inertial and dissipative forcings on the rhs—leads to an alternative perturbation form of the momentum equation

$$\begin{aligned} \frac{d\mathbf{u}'}{dt} = & -\mathbf{v}' \cdot \nabla \mathbf{u}_a - \frac{\theta}{\theta_0} \widetilde{\mathbf{G}} \nabla \phi' - \mathbf{g} \frac{\theta'}{\theta_a} - \mathbf{f} \times \left( \mathbf{u} - \frac{\theta}{\theta_a} \mathbf{u}_a \right) \\ & + \left( \mathbf{M}(\mathbf{u}) - \frac{\theta}{\theta_a} \mathbf{M}(\mathbf{u}_a) \right) + \left( \mathbf{D}(\mathbf{u}) - \frac{\theta}{\theta_a} \mathbf{D}(\mathbf{u}_a) \right) + \frac{\theta'}{\theta_a} \frac{d_a \mathbf{u}_a}{dt}, \end{aligned} \quad (10)$$

where  $\mathbf{u} = \mathbf{u}' + \mathbf{u}_a$  is utilised on the rhs. Furthermore, moving the first term on the rhs of (10) to the lhs, then using (6a) and then moving  $d\mathbf{u}_a/dt$  back to the rhs to combine it with the last term, produces

$$\begin{aligned} \frac{d\mathbf{u}}{dt} = & -\frac{\theta}{\theta_0} \widetilde{\mathbf{G}} \nabla \phi' - \mathbf{g} \frac{\theta'}{\theta_a} - \mathbf{f} \times \left( \mathbf{u} - \frac{\theta}{\theta_a} \mathbf{u}_a \right) \\ & + \left( \mathbf{M}(\mathbf{u}) - \frac{\theta}{\theta_a} \mathbf{M}(\mathbf{u}_a) \right) + \left( \mathbf{D}(\mathbf{u}) - \frac{\theta}{\theta_a} \mathbf{D}(\mathbf{u}_a) \right) + \frac{\theta}{\theta_a} \frac{d_a \mathbf{u}_a}{dt}. \end{aligned} \quad (11)$$

The latter form is already familiar from [35,36]—cf. eqs. (39) and (1c), respectively, in [35] and [36]—where it was used for the special case of the thermally balanced zonal wind (inviscid) in (3) implying  $d_a \mathbf{u}_a/dt \equiv 0$  and  $\mathbf{D}(\mathbf{u}_a) \equiv 0$  on the lhs and rhs of (3c), respectively. Moreover, the process of navigating from (7b) to (11) suggests yet another form

$$\begin{aligned} \frac{d\mathbf{u}}{dt} = & -\frac{\theta}{\theta_0} \widetilde{\mathbf{G}} \nabla \phi' - \frac{\theta'}{\theta_0} \widetilde{\mathbf{G}} \nabla \phi_a - \mathbf{f} \times (\mathbf{u} - \mathbf{u}_a) \\ & + (\mathbf{M}(\mathbf{u}) - \mathbf{M}(\mathbf{u}_a)) + (\mathbf{D}(\mathbf{u}) - \mathbf{D}(\mathbf{u}_a)) + \frac{d_a \mathbf{u}_a}{dt}, \end{aligned} \quad (12)$$

a variant of (11) formulated in terms of the generalised buoyancy or, alternatively, a variant of (7b) formulated in terms of full velocity rather than its perturbations.

### 2.3.2 Discussion

The four perturbation forms of the momentum equation (7b), (10), (11) and (12) are mathematically equivalent, as their derivations only manipulate selected terms in the equations and redefine dependent variables. From the perspective of numerical approximations, however, different forms enable novel

algorithmic designs, with (7b) promising greater efficacy, especially in the context of “long or fussy integrations” [19]. Because of the aforementioned specificity of global atmospheric flows, our focus is on two-time-level nonoscillatory forward-in-time (NFT) integrators, implicit with respect to acoustic, buoyant, and rotational modes. At the highest level, the NFT template represents the problem solution as a sum of explicit and implicit terms,

$$\boldsymbol{\psi}_i^{n+1} = \mathcal{A}_i(\boldsymbol{\psi}^n + 0.5\delta t \mathcal{R}(\boldsymbol{\psi}^n)) + 0.5\delta t \mathcal{R}_i(\boldsymbol{\psi}^{n+1}) \equiv \widehat{\boldsymbol{\psi}}_i + 0.5\delta t \mathcal{R}_i(\boldsymbol{\psi}^{n+1}) \quad (13)$$

where  $\boldsymbol{\psi}$  symbolises the vector of dependent variables ( $\mathbf{u}, \theta, \phi, \rho$ ) or perturbations thereof,  $n$  and  $\mathbf{i}$  refer to the temporal and spatial position on a discretisation mesh,  $\mathcal{A}$  symbolises a NFT advective transport operator, and  $\mathcal{R}$  marks the cumulative forcings on the rhs of the PDE system at hand. The template (13) is common for both the advective ( $d\boldsymbol{\psi}/dt = \mathcal{R}$ ) and the conservative ( $\partial \mathcal{G}\rho\boldsymbol{\psi}/\partial t + \nabla \cdot \mathcal{G}\rho\mathbf{v}\boldsymbol{\psi} = \mathcal{G}\rho\mathcal{R}$ ) forms of the governing equations. In the former case, (13) represents a class of trajectory-wise semi-Lagrangian integrators, whereas in the latter case it refers to a class of control-volume-wise Eulerian integrators. Generally,  $\mathcal{R}$  is composed of linear and nonlinear complements in terms of  $\boldsymbol{\psi}$ . The nonlinear elements are explicitly predicted at  $n + 1$ , upon which all linear terms are treated implicitly. This class of algorithms—widely-documented in the literature, see [35,36] and references therein—benefits both computational stability and accuracy of discrete integrations. In particular, the adopted trapezoidal-rule integration of all restoring forces is free of amplitude errors, which is especially important for representing slow oscillations and wave phenomena in geo/astrophysical systems [43,4,32,45,8,24], and different perturbation forms encourage different level of implicitness in determining final solutions for  $\boldsymbol{\psi}^{n+1}$ .

Among (7b), (10), (11) and (12), (7b) implies integrators with the highest degree of implicitness as, except for the coefficient of the pressure gradient and the metric forcing, the remaining rhs can be viewed as an action of a linear operator on the vector of the perturbation variables ( $\mathbf{u}', \phi', \theta'$ ). There are two noteworthy aspects of (7b). One is the convective derivative of the ambient velocity component analogous to the convective derivative of the ambient potential temperature in (7a). The other is the vectorial buoyancy term,  $\propto \theta'$ , appearing in all three components of the momentum equation. This contrasts with (11), familiar from solving implicitly for the full velocity with buoyancy standardly confined to the vertical (viz. radial on the sphere) component equation aligned with  $\mathbf{g}$ . Furthermore, all coefficients  $\theta/\theta_a$  on the rhs of (11) are predicted explicitly at  $t^{n+1}$ . The form (10) is intermediate between (7b) and (11), in that it retains many aspects of the familiar design while still solving for the velocity perturbations. Conversely, (12) retains the generalised buoyancy of (7b) while solving for the full velocity. The ability of solving all four forms is useful for assessing the relative importance of various terms and balances in numerical integrations. In the following, we shall focus on the complete de-

scription of (7b), as it appears the most promising in terms of computational efficacy and implementation flexibility while revealing the most challenging elliptic Helmholtz problem associated with the implicit integration procedure. Furthermore, having an effective integrator for (7b) enables incorporation of the other three options in the same model code with relative ease.

### 3 NUMERICAL APPROXIMATIONS

#### 3.1 Semi-implicit integrators

The system of PDEs based on (1a), (7a) and (7b) is cast in the conservation form

$$\frac{\partial \mathcal{G}\rho}{\partial t} + \nabla \cdot (\mathcal{G}\rho\mathbf{v}) = 0, \quad (14a)$$

$$\frac{\partial \mathcal{G}\rho\theta'}{\partial t} + \nabla \cdot (\mathcal{G}\rho\mathbf{v}\theta') = -\mathcal{G}\rho \left( \tilde{\mathbf{G}}^T \mathbf{u}' \cdot \nabla \theta_a - \mathcal{H}' - \alpha^\theta \theta' \right), \quad (14b)$$

$$\begin{aligned} \frac{\partial \mathcal{G}\rho\mathbf{u}'}{\partial t} + \nabla \cdot (\mathcal{G}\rho\mathbf{v} \otimes \mathbf{u}') = & -\mathcal{G}\rho \left( \tilde{\mathbf{G}}^T \mathbf{u}' \cdot \nabla \mathbf{u}_a + \frac{\theta}{\theta_0} \tilde{\mathbf{G}} \nabla \phi' + \frac{\theta'}{\theta_0} \tilde{\mathbf{G}} \nabla \phi_a \right. \\ & \left. + \mathbf{f} \times \mathbf{u}' - \mathcal{M}'(\mathbf{u}, \mathbf{u}_a) - \mathcal{D}'(\mathbf{u}, \mathbf{u}_a) - \alpha^u \mathbf{u}' \right), \end{aligned} \quad (14c)$$

and consistently augmented with the relaxation terms  $-\alpha^\theta \theta'$  and  $-\alpha^u \mathbf{u}'$  in the entropy and momentum equation, respectively. These numerical devices simulate, e.g. wave absorbing devices in the vicinity of the open boundaries [27] and/or immersed solids [31], or provide a basic tool for time-continuous data assimilation [3]. The coefficients  $\alpha^\theta$  and  $\alpha^u$ —generally, functions of  $(\mathbf{x}, t)$ —represent inverse time-scales for the relaxation of actual potential temperature and velocity fields towards their ambient values. Although numerically motivated, these devices are treated consistently with physical forcings and need to be rigorously accounted for in the construction of semi-implicit integrators; cf. Appendix A in [22].

The semi-implicit integrator of the system (14) adopts the general NFT template (13) following the procedure detailed in [35,36]. This procedure commences with integration of the mass continuity equation (14a) as

$$\rho_{\mathbf{i}}^{n+1} = \mathcal{A}_{\mathbf{i}} \left( \rho^n, (\mathbf{v}\mathcal{G})^{n+1/2}, \mathcal{G}^n, \mathcal{G}^{n+1} \right) \implies \mathbf{V}^{n+1/2} = \overline{\mathbf{v}^\perp \mathcal{G} \rho}^{n+1/2} \quad (15)$$

where  $\mathcal{A}$  denotes a bespoke multidimensional positive definite advection transport algorithm (MPDATA) for compressible atmospheric flows [13], a hybrid [36] of structured-grid [30] and unstructured-mesh [29] schemes for the vertical and horizontal discretisations. Given the provision of a first-order accurate

estimate of the advector  $(\mathbf{v}\mathcal{G})^{n+1/2}$  at the intermediate time level  $t^{n+1/2}$ ,  $\mathcal{A}_i$  provides a second-order accurate solution for  $\rho_i^{n+1} \forall \mathbf{i}$ , together with the cumulative face-normal advective mass fluxes  $\mathbf{V}^{n+1/2}$ . These advective mass fluxes and the updated density  $\rho^{n+1}$  are subsequently applied in the integration of (14b) and (14c) following (13). Namely,

$$\theta_i'^{n+1} = \widehat{\theta}'_i - 0.5\delta t \left( \widetilde{\mathbf{G}}^T \mathbf{u}'^{n+1} \cdot \nabla \theta_a^{n+1} + \alpha^\theta \theta'^{n+1} \right)_i \quad (16a)$$

$$\begin{aligned} \mathbf{u}'_i^{n+1} = & \widehat{\mathbf{u}}'_i - 0.5\delta t \left( \widetilde{\mathbf{G}}^T \mathbf{u}'^{n+1} \cdot \nabla \mathbf{u}_a^{n+1} \right)_i \\ & - 0.5\delta t \left( \frac{\theta^\star}{\theta_0} \widetilde{\mathbf{G}} \nabla \phi'^{n+1} + \frac{\theta'^{n+1}}{\theta_0} \widetilde{\mathbf{G}} \nabla \phi_a^{n+1} \right)_i \\ & - 0.5\delta t \left( \mathbf{f} \times \mathbf{u}'^{n+1} - \mathcal{M}'(\mathbf{u}'^\star, \mathbf{u}_a^{n+1}) + \alpha^u \mathbf{u}'^{n+1} \right)_i, \end{aligned} \quad (16b)$$

where:

$$\widehat{\theta}'_i = \mathcal{A}_i \left( \widetilde{\theta}', \mathbf{V}^{n+1/2}, (\rho\mathcal{G})^n, (\rho\mathcal{G})^{n+1} \right), \quad \widetilde{\theta}' = \left( \theta' + 0.5\delta t \mathcal{R}^\theta \right)^n; \quad (17a)$$

$$\widehat{\mathbf{u}}'_i = \mathcal{A}_i \left( \widetilde{\mathbf{u}}', \mathbf{V}^{n+1/2}, (\rho\mathcal{G})^n, (\rho\mathcal{G})^{n+1} \right), \quad \widetilde{\mathbf{u}}' = \left( \mathbf{u}' + 0.5\delta t \mathcal{R}^u \right)^n; \quad (17b)$$

and where superscript  $\star$  on the rhs of (16b) refers to explicit predictors executed iteratively and lagged behind the linear terms; see section 3.2 in [36]. Furthermore, the perturbation heat source  $\mathcal{H}'$  has been included in the  $\theta'$  argument of the transport operator, by adopting the  $\mathcal{R}^\theta = \widetilde{\mathbf{G}}^T \mathbf{u}' \cdot \nabla \theta_a + 2\mathcal{H}'$  representation at  $t^n$ . Analogously,  $\mathcal{R}^u$  subsumes the perturbation dissipation term  $2\mathcal{D}'$ .

The integrator outlined in (16) contains fully implicit trapezoidal integrals of generalised buoyancy, Coriolis and relaxation terms, whereas trapezoidal integrals of the nonlinear terms of pressure-gradient and metric forcings employ explicit predictors of full potential temperature and velocity, respectively. The derivation of the closed-form expression for the velocity update is involving. The overall idea is to substitute the potential temperature in the generalised buoyancy term of (16b) with the rhs of the entropy integral (16a) and gather all terms depending on  $\mathbf{u}^{n+1}$  on the lhs of the momentum integral, upon which the closed-form expression for velocity update emerges as an inversion of a linear problem. To simplify the notation, in the following the spatial position index  $\mathbf{i}$  is dropped everywhere, as all dependent variables, coefficients and terms are co-located in (16). Similarly, the temporal index  $n + 1$  is also dropped, as there is no ambiguity. Furthermore, the ratios of the potential temperature and its reference value are subsequently referred to as  $\theta/\theta_0 = \Theta$ , whereas  $\delta_h t = 0.5\delta t$ . Because further derivations require an intricate component representation of the vector equation (16b), we adopt the notations  $\mathbf{u} = (u^x, u^y, u^z)$

and  $\widetilde{\mathbf{G}}\nabla = \widetilde{\nabla} = (\widetilde{\partial}_x, \widetilde{\partial}_y, \widetilde{\partial}_z)$ .<sup>1</sup> We also note the auxiliary relation

$$\forall \psi, \quad (\widetilde{\mathbf{G}}^T \mathbf{u}) \cdot \nabla \psi = \mathbf{u} \cdot (\widetilde{\mathbf{G}}\nabla \psi) \equiv \mathbf{u} \cdot \widetilde{\nabla} \psi, \quad (18)$$

and define two auxiliary parameters

$$\tau^\theta := \delta_{ht} (1 + \delta_{ht} \alpha^\theta)^{-1}, \quad \tau^u := \delta_{ht} (1 + \delta_{ht} \alpha^u)^{-1}. \quad (19)$$

With these simplifications (16a) can be rewritten as

$$\Theta' = \frac{\tau^\theta}{\delta_{ht}} \left( \widehat{\Theta}' - \delta_{ht} \mathbf{u}' \cdot \widetilde{\nabla} \Theta_a \right), \quad (20)$$

upon which (16b) can be rearranged as

$$\begin{aligned} \mathbf{u}' + \tau^u \mathbf{u}' \cdot \widetilde{\nabla} \mathbf{u}_a + \tau^u \mathbf{f} \times \mathbf{u}' - \tau^u \tau^\theta \left( \mathbf{u}' \cdot \widetilde{\nabla} \Theta_a \right) \widetilde{\nabla} \phi_a \\ = \widehat{\mathbf{u}}' - \tau^u \Theta^* \widetilde{\nabla} \phi'. \end{aligned} \quad (21)$$

where the resulting explicit part of the velocity solution is

$$\widehat{\mathbf{u}}' = \frac{\tau^u}{\delta_{ht}} \left( \widehat{\mathbf{u}}' - \tau^\theta \widehat{\Theta}' \widetilde{\nabla} \phi_a + \delta_{ht} \mathbf{M}'(\mathbf{u}^*, \mathbf{u}_a) \right). \quad (22)$$

The implicit (in  $\mathbf{u}'$ ) equation (21) reveals the linear problem

$$\mathbf{L} \mathbf{u}' = \widehat{\mathbf{u}}' - \tau^u \Theta^* \widetilde{\nabla} \phi' \implies \quad (23a)$$

$$\mathbf{u}' = \check{\mathbf{u}}' - \mathbf{C} \nabla \phi'; \quad \check{\mathbf{u}}' = \mathbf{L}^{-1} \widehat{\mathbf{u}}', \quad \mathbf{C} = \tau^u \Theta^* \mathbf{L}^{-1} \widetilde{\mathbf{G}}, \quad (23b)$$

cf. §3.2 in [36]. The implied inverse (23b) provides closed-form expression for the perturbation velocity update, provided the availability of  $\phi'$ . For the acoustic scheme that resolves propagation of sound waves,  $\phi'$  directly derives from the gas law (2), and so (23b) basically completes the solution [35]. For semi-implicit integrators that admit soundproof time steps, the closed-form expression for  $\mathbf{u}'$  in (23b) is a necessary prerequisite of the elliptic boundary value problem at the heart of the FVM [35,36]. The key element of (23b) is the linear operator  $\mathbf{L}$ , from which  $\mathbf{L}^{-1}$  and  $\mathbf{C}$  straightforwardly follow. Because (21) differs from all NFT semi-implicit forms presented in the past [25,27,22], the details of  $\mathbf{L}$  are fully documented in Appendix B, whereas formulating the elliptic pressure equation is discussed next.

<sup>1</sup> Consider that each  $\widetilde{\partial}$  is composed of three terms; e.g.  $\widetilde{\partial}_x = g_{11}\partial_x + g_{12}\partial_y + g_{13}\partial_z$ , where  $g_{ij}$  are entries of  $\widetilde{\mathbf{G}}$ .

### 3.2 Elliptic boundary value problem

#### 3.2.1 Seasoned formulation

The boundary value problem (BVP) for  $\varphi \equiv \phi'$  supersedes (2) with its advective form  $d(\text{Eq.2})/dt$  that, when integrated consistently with the model numerics, can ensure computational stability independent of the speed of sound [35,15,36,37]. In particular, recalling from §2.1 that  $\mathbf{v} = \widetilde{\mathbf{G}}^T \mathbf{u}$ , (23) entails

$$\mathbf{v} = \check{\mathbf{v}} - \widetilde{\mathbf{G}}^T \mathbf{C} \nabla \varphi, \quad \text{with } \check{\mathbf{v}} = \widetilde{\mathbf{G}}^T \check{\mathbf{u}} \equiv \widetilde{\mathbf{G}}^T (\check{\mathbf{u}}' + \mathbf{u}_a), \quad (24)$$

whereby  $d/dt(2)$  leads to the PDE

$$\frac{\partial \mathcal{G} \rho \varphi}{\partial t} + \nabla \cdot (\mathcal{G} \rho \mathbf{v} \varphi) = \mathcal{G} \rho \sum_{\ell=1}^3 \left( \frac{a_\ell}{\zeta_\ell} \nabla \cdot \zeta_\ell (\check{\mathbf{v}} - \widetilde{\mathbf{G}}^T \mathbf{C} \nabla \varphi) \right) + b\varphi + c, \quad (25)$$

where coefficients  $a_\ell$ ,  $b$ ,  $c$  may depend on  $\varphi$  but the modified densities  $\zeta_\ell$  are explicitly known. The PDE (25) is integrated to  $\mathcal{O}(\delta t^2)$  with a mixed forward/backward variant of the template algorithm (13)

$$\varphi_i^{n+1} = \mathcal{A}_i \left( \tilde{\varphi}, \mathbf{V}^{n+1/2}, \rho^{*n}, \rho^{*n+1} \right) + \delta t \widetilde{\mathcal{R}} \varphi|_i^{n+1} \equiv \hat{\varphi}_i + \delta t \widetilde{\mathcal{R}} \varphi|_i^{n+1}, \quad (26)$$

where  $\widetilde{\mathcal{R}} \varphi \equiv [\text{rhs}(25) - (b\varphi + c)]/\mathcal{G}\rho$  denotes the implicit forcing composed of the three divergence operators on the rhs of (25), while  $\tilde{\varphi} = [\varphi + \delta t(b\varphi + c)]^n$  under  $\mathcal{A}$  combines the past pressure perturbation with the explicit thermodynamic forcing; cf. [36,37] for details. Altogether, the template (26) provides a discrete implicit constraint for (24), and thus for (23b),<sup>2</sup>

$$0 = - \sum_{\ell=1}^3 \left( \frac{A_\ell^*}{\zeta_\ell} \nabla \cdot \zeta_\ell (\check{\mathbf{v}} - \widetilde{\mathbf{G}}^T \mathbf{C} \nabla \varphi) \right) - B^*(\varphi - \hat{\varphi}). \quad (27)$$

The coefficients  $A^*$  and  $B^*$  in (27) result from coefficients  $a_\ell$  in (25) and the superscript  $\star$  indicates that their dependence on  $\varphi$  is lagged. The Helmholtz problem (27) was discussed in [35,15]. In NFT codes, we solve (27) with a bespoke nonsymmetric preconditioned Generalised Conjugate Residual (GCR) approach, widely discussed in the literature; see [33] for a recent overview and a comprehensive list of references. The solution of (27) provides updated pressure perturbation variable  $\varphi$  that subsequently completes the solution for  $\mathbf{v}$  in (24) and  $\mathbf{u}' = [\widetilde{\mathbf{G}}^T]^{-1} \mathbf{v} - \mathbf{u}_a$ . This completes the theory of the new perturbation equations and their semi-implicit NFT integrators.

<sup>2</sup> Taking the differential of an ideal gas law (2), and using  $R = c_p - c_v$ , leads to  $c_v dT = T c_p d \ln \theta - p d(1/\rho)$ ; so (27) amounts to an internal energy constraint.

### 3.2.2 Implementation

The formulation of the BVP (27) summarised above retains the structure of the analogous BVP established for the “full-velocity” integrators of (11) advanced in [35,36]. Taking into account the substantial complexity of the new perturbation approach, retaining this structure minimises the burden of reformulating the NFT model solver, in essence, to the re-specification of the explicit vector field and the fields of coefficients that enter the semi-implicit integrator and the BVP, while leaving intact the elliptic solver per se and its elaborate boundary conditions, generally imposed along time-dependent curvilinear boundaries [22,42,28,11,35]. However, notwithstanding the compact symbolic representation of the linear operators  $\mathbf{L}$ ,  $\mathbf{L}^{-1}$ , and  $\mathbf{C}$  outlined above, programming the optimal computational representation of (27), is still demanding. The goal is to minimise the round-off error and computational expense implied by straightforward matrix operations of Appendix B, by taking advantage of numerous analytic cancellations and judicious rearrangements to minimise floating point operations of the implicit solver.

The common molecule  $\zeta_\ell^{-1} \nabla \cdot \zeta_\ell (\check{\mathbf{v}} - \widetilde{\mathbf{G}}^T \mathbf{C} \nabla \varphi)$  of the three Poisson operators in (27), can be computationally intensive and, thus, determining the complexity and the computational cost of evaluating the generalised Helmholtz operator. Following Appendix A of [22], this molecule forms with accuracy to a multiplicative factor the elliptic Poisson equation for the anelastic PDEs evaluated as

$$\frac{1}{\zeta_\ell} \frac{\partial}{\partial x^j} \left[ \zeta_\ell \mathcal{E} \left( \widetilde{\mathcal{V}}^j - \widetilde{\mathcal{E}}^{jk} \frac{\partial \varphi}{\partial x^k} \right) \right] = 0, \quad (28)$$

where  $j, k = 1, 2, 3$ , repeating indices indicate summation, and functions  $\widetilde{\mathcal{V}}^j$  and  $\widetilde{\mathcal{E}}^{jk}$  are

$$\widetilde{\mathcal{V}}^j = \widetilde{G}_p^j \mathcal{V}^p, \quad \widetilde{\mathcal{E}}^{jk} = \widetilde{G}_p^j \mathcal{E}^{pk}; \quad p = 1, 2, 3. \quad (29)$$

Here, scalar fields  $\widetilde{G}_p^j$  correspond to the entries  $g_{pj}$  of the matrix  $\widetilde{\mathbf{G}}^T$ , while  $\mathcal{V}^p$  and  $\mathcal{E}^{pk}$  are specified in detail in Appendix A of [22] for the anelastic system [18] cast in a generalised curvilinear framework common to EULAG and FVM. However, thanks to the coefficient field  $\mathcal{E}$  the operator on the lhs can accommodate equally well the pseudo-incompressible [6] and fully compressible Euler equations discussed in this paper. For instance, in the latter case

$$\mathcal{E} \widetilde{\mathcal{V}}^j \equiv \check{\mathbf{v}}^j \equiv \widetilde{G}_p^j \check{\mathbf{u}}^p, \quad \mathcal{E} \widetilde{\mathcal{E}}^{jk} \equiv [\widetilde{\mathbf{G}}^T \mathbf{C}]_{jk} \quad (30)$$

that de facto redefines the  $\widetilde{\mathcal{V}}^j$  and  $\widetilde{\mathcal{E}}^{jk}$  input to the solver as the reciprocals of the respective rhs in (30) and the scalar field  $\mathcal{E}$ . In principle there is substantial freedom in defining  $\mathcal{E}$ , but its purpose is to factor out the greatest common

factor of all entries  $[\widetilde{\mathbf{G}}^T \mathbf{C}]_{jk}$ ; e.g.  $\mathcal{E} \propto \Theta^* \{\mathbf{L}\}^{-1}$ , as suggested by the forms of  $\mathbf{C}$  and  $\mathbf{L}^{-1}$  specified in (23b) and Appendix B, respectively.

With the given design, all explicit elements of the molecule (28) need to be calculated once per call of the elliptic solver; whereas in calculations with fixed geometry and constant time step, all  $\widetilde{\mathcal{E}}^{jk}$  coefficients can be precomputed at the model initialisation. In the next section, the examples of applications will be shown for the perturbation forms (7b), (10), (11) and (12) assuming geostrophically balanced ambient states

$$[\rho_a, \theta_a, \phi_a, \mathbf{u}_a] = [\rho_a(y, z), \theta_a(y, z), \phi_a(y, z), (u_a(y, z), 0, 0)] . \quad (31)$$

Even such a simple ambient state adds complexity to existing codes that employ (28). The interested reader is referred to Appendix C, where a complete description of (28) is provided for the selected class of ambient states (31).

## 4 RESULTS

### 4.1 Preamble

Herein we verify the theoretical developments of the preceding sections, the prospective goal of which is to extend the reliable range of simulations of weather and climate that depend on both initial and boundary conditions. Here, we do not anticipate spectacular differences between the solutions generated with the established all-scale compressible Euler equations and their newly developed perturbation forms, simply because the established equations are already proven to provide quality solutions in state-of-the-art weather-prediction models [14]. Our objective is to verify that the new perturbation forms reproduce the established solutions for shorter integration times at the equivalent computational cost, and to look for hints indicating the potential of the new forms for extending the range and reliability of numerical weather prediction. We demonstrate this with an evolution of planetary baroclinic instability that epitomises life cycles of natural weather systems in mid-latitudes, while being well studied theoretically and numerically. In particular, we extend the range of the adopted benchmark [40] and follow the description in the 2016 edition of DCMIP (Dynamical Core Model Intercomparison Project) [41].

To illustrate the results using the different semi-implicit integrators that stem from alternate perturbation formulations of the all-scale compressible Euler equations, we compare the numerical solutions to the systems (7b), (10), (11) and (12); hereafter referred to as GBIS, IS, REF and GB—for “generalised

buoyancy and implicit shears”, “implicit shears”, “reference” and “generalised buoyancy”, respectively. Rather than focusing on the results up to day 10, we look at later solutions when the flow transition to geophysical turbulence and the different equation sets and models start diverging. Comparing extended-range solutions is currently not considered in model intercomparisons [40].

#### 4.2 *Baroclinic instability*

The adopted basic setup assumes a dry, inviscid and adiabatic, deep atmosphere with two mid-latitude zonal jets symmetric about the equator, in thermal wind balance with the meridional temperature distribution. A localised zonal velocity perturbation in the form of a simple exponential bell (tapered to zero in the vertical) excites the instability, leading to eastward propagating Rossby modes. After about 8 days of integration, the baroclinic wave breaks and forms sharp fronts in the lower troposphere, whereas after 15 days the flow in the region of the northerly jet becomes turbulent. Notwithstanding, after 15 days the results of all conducted simulations match each other closely—within 10% of the solution amplitude—regardless of the selected equations, and are hardly distinguishable by eye. However three days later, the analogous solutions evince departures sufficiently large to substantiate the significance of the new equations.

On the numerical side, the simulations resolve spherical surfaces with the median-dual finite-volume mesh developed about the nodes of the octahedral reduced Gaussian grid [36]. The associated primary mesh is composed of triangular and quadrilateral elements as illustrated in, e.g. Fig. 2 of [13]—the dual mesh associated with this primary mesh consists of general polygons. For computational economy, the discussion is focused on a series of experiments using the O180 octahedral reduced Gaussian grid, corresponding to a quasi-uniform mesh spacing of about 55 km, and only selected two experiments are shown for the analogous O640 reduced Gaussian grid, with mesh spacing of about 16 km.<sup>3</sup> In the vertical, the discretisation is structured and uniform in computational space. Stretched smoothly by means of continuous mappings, the vertical grid in physical space resolves a 44.25 km deep domain with 59 intervals varying from a minimum of 84 m near the surface to 1690 m near the model top. The variable time step targets the maximum advective Courant number 0.95—the time step for the O180 grid varied from 1200 s during the first 6 days to 375 s towards the end of the 20 day simulation. The calculations are explicitly inviscid, delegating the solution regularisation at the mesh resolution to nonoscillatory properties of the MPDATA based integrators.

---

<sup>3</sup> The octahedral reduced Gaussian grid is special, in that it also supports spherical harmonics transforms [36].

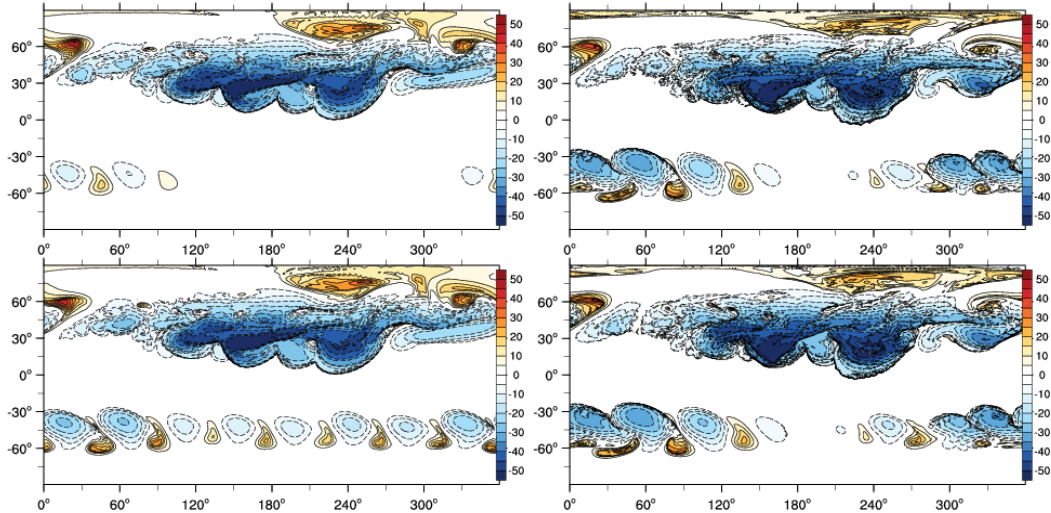


Fig. 1. Surface potential temperature perturbation  $\theta'$  after 18 simulated days. The solutions GBIS and REF, corresponding to perturbation equations (7b) and (11) are shown at the top and bottom, respectively. The results from the O180 and O640 mesh are shown on the left and right, correspondingly.

Figure 1 shows  $\theta'$  at the surface ( $z = 0$ ) after 18 days of the instability evolution for the GBIS and REF solutions to (7b) and (11), respectively, in the top and bottom row. The IS and GB solutions to (10) and (12), respectively, are not displayed as IS (GB) closely corresponds to the GBIS (REF) results, due to the dominant role of the vertical shear of the ambient flow; cf. Fig 1 in [40]. The O180 results in the left column are supplemented with the corresponding higher-resolution O640 results in the right column. In terms of the overall pattern, the GBIS and REF solutions match each other closely, and their relative departures appear confined to details, except for the more advanced development of the instability in the southern hemisphere for the O180 reference solution, visibly diminished towards the GBIS result at O640 resolution. Although this somewhat delayed development of the instability in the southern hemisphere appears consistent with the intent of the IS design—to mitigate spurious nonlinear interactions of balanced ambient flows with truncation errors of advection schemes and to possibly capture energy cascades with greater accuracy—its actual cause is unclear.

The southern hemisphere instability onset was used as a criterion in the HI-WPP [9] dynamical core intercomparison to illustrate the impact of increased truncation errors near irregularities of the computational mesh. After day 8 when the wave breaks, the nonlinear effects become important and various model predictions tend to diverge afterwards. In particular, the overall gentle excitation of the instability on the southern hemisphere—physically due to the gravity waves radiating from the baroclinic eddies in the northern hemisphere—can be easily accelerated by the errors (truncation or round-off) of numerical approximations; cf. Section 5e in [10] for a discussion. To assess

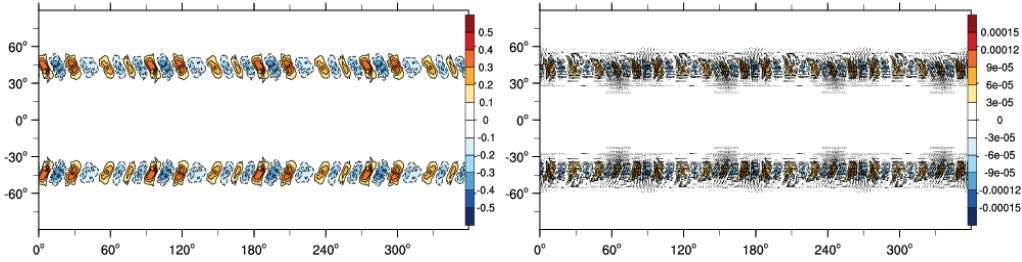


Fig. 2. The 18 days surface  $\theta'$  REF (left) and GBIS (right) solutions on the O180 grid without the initial perturbation.

the role of discretisation errors due to irregularity of the mesh, we repeat the O180 experiment but with zero initial perturbations on both hemispheres. Because the discretisation in the horizontal is unstructured, partial derivatives in the zonal and meridional directions are evaluated from the Gauss divergence theorem [36], using the same area stencil. In consequence, they do not identically vanish for uniform fields in the zonal and meridional directions, respectively. This leads to the so-called grid imprinting, which can provide sufficient perturbations to excite the instability. The REF and GBIS solutions without initial perturbations are shown in Fig. 2 for the O180 mesh. The corresponding O640 mesh results are undisplayable, as they reflect a gridscale noise concentrated about four special points on each hemisphere—detectable in the left panel by wider negative perturbations at the approximate locations of  $30^\circ$ ,  $120^\circ$ ,  $210^\circ$  and  $300^\circ$ —with the (average; standard deviation) measures of  $(2.2 \times 10^{-4}; 2.4 \times 10^{-2})$  and  $(2.7 \times 10^{-11}; 7.4 \times 10^{-6})$ , respectively, for REF and GBIS solutions. Altogether, the potential temperature perturbations in simulations without initial perturbations, are at least two and five orders of magnitude smaller, for REF and GBIS respectively, than with the initial perturbations applied. This together with the wavelength roughly corresponding to the fastest growing mode of the baroclinic instability attests that the excitation of the instability in the southern hemisphere is likely due to the resolved global flow, whose later evolution proceeds differently in the GBIS and REF results due to different behavioural errors of their corresponding solvers. Importantly, however, the magnitude of the grid imprinting is four orders of magnitude smaller in the GBIS solution than in the REF solutions.

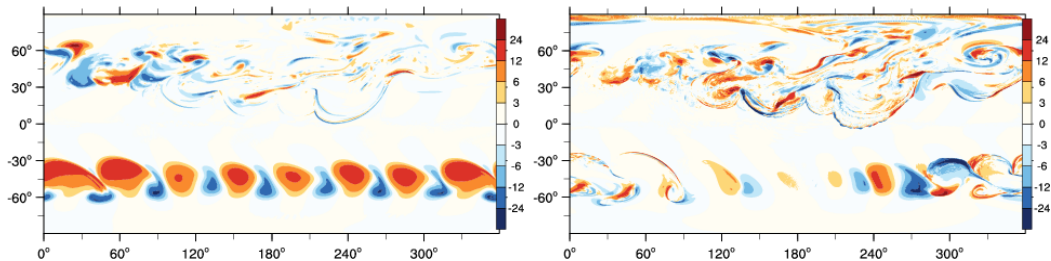


Fig. 3. GBIS-REF differences of the  $\theta'$  solutions in Fig. 1.

The difference plots in Fig. 3 quantify the GBIS-REF differences of the solutions in Fig. 1, using a bespoke nonlinear colour scale that covers about half

the range of the solution amplitude  $\sim 50\text{K}$ . While the overall differences are comparable with the signal amplitude (approximately within 50% of the amplitude) for both resolutions employed in Fig. 1, there are conspicuous departures of the differences per se between the two resolutions. At lower resolution, the GBIS-REF departures emphasize "turbulent" trailing edge—followed by the leading edge due to zonal periodicity—of the northern baroclinic wave train and the growing instability in the southern hemisphere. At the higher resolution these departures diminish in favour of sharp frontal structures in the northern hemisphere. Consider that after 10 days—cf. section 6.2 in [13]—these same differences are only within 1% of the solution amplitude at both resolutions. For reference, the magnitude of the differences resulting from only stochastic (i.e. no initial) perturbations applied to the physical parametrizations in ECMWF’s ensemble system [17] are typically 1% over a 48 hour forecast period when comparing control and perturbed forecasts for selected parameters. Consequently, the effects due to the alternate perturbation equations are altogether subtle but potentially significant.

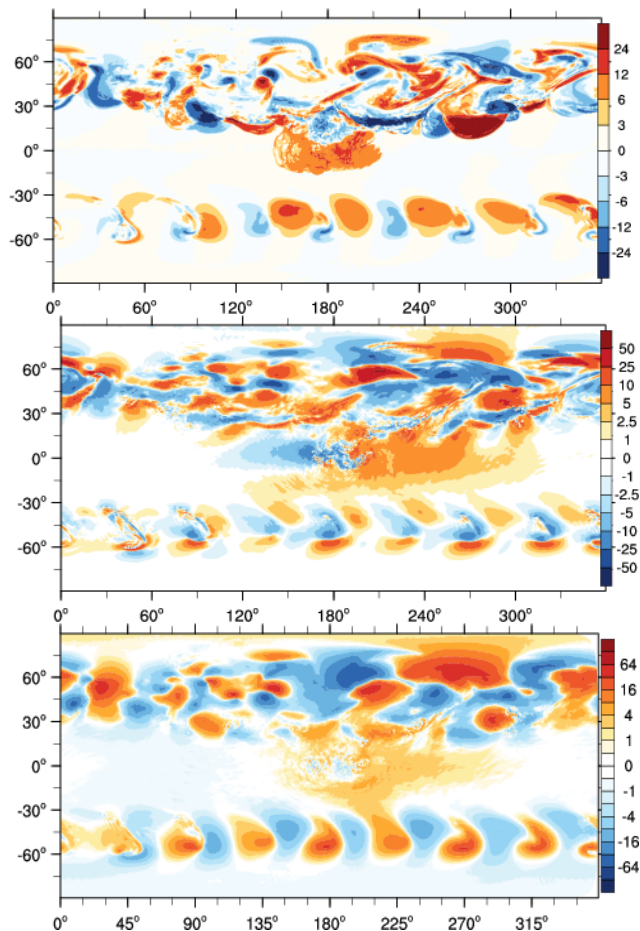


Fig. 4. The difference GBIS minus REF for surface potential temperature (top), zonal wind [m/s] at 850hPa (centre) and surface pressure [hPa] (bottom) of the 18 days moist solutions.

Adding moisture to the problem [41] invigorates the evolution of the baroclinic eddies and increases the solution uncertainty [47,12].<sup>4</sup> This is evidenced in Fig. 4 that show the GBIS-REF differences for 18 days moist solutions corresponding to that shown in the left column of Fig. 3, supplied with plots of zonal wind at 850hPa and surface pressure. The differences between the moist GBIS and REF results are more apparent. In the northern hemisphere they are primarily correlated with the steep fronts of the overturning eddies (viz. advanced nonlinearity). In the southern hemisphere, the persistently more advanced development of the instability in the REF solution is still evident. Because moisture substantially complicates gravity wave dynamics [5,1] and energises spectra in small scales [16], susceptible to truncation and round-off errors, the consistency of the moist results with the dry solutions indicates the dominant role of planetary-scale modulation in retarding the southern hemispheric evolution in the GBIS result. The zonal wind at 850hPa and surface pressure are both weather evolution relevant parameters and clearly indicate planetary-scale differences.

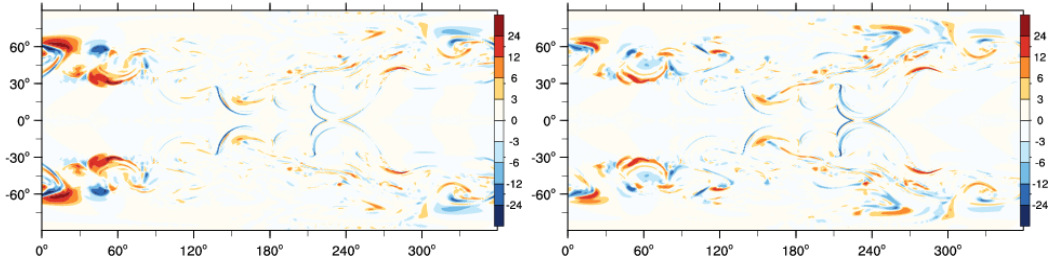


Fig. 5. GBIS-REF departures of the 18 days surface  $\theta'$  solutions on the O180 grid for the symmetrically excited instability. Left and right panels show, respectively, the solutions with one (default) and two outer iterations in (16b) and (27).

To further substantiate the improved accuracy of the GBIS solutions for global weather evolution, we perturb the zonal jets symmetrically on both hemispheres. There are two distinct aspects of this experiment. On the numerical side, the results verify the cross-equatorial symmetry of the numerical solutions, thereby exposing the solution departures solely due to the truncation errors. On the physical side, the results are more relevant to real weather, continuously forced on both hemispheres. In terms of truncation errors, the GBIS solutions are by design more accurate and less dissipative than the REF solutions (recall the discussion in section 2.3.2). In particular, the semi-implicit integrators (16) for GBIS more broadly rely on the trapezoidal integrals, whereby there are fewer lagged coefficients—marked with  $\star$  in (16b) and (27)—in the outer iteration that improves the explicit estimates in the non-linear terms. While all simulations discussed so far used one (default) outer iteration, the current experiment was also conducted with two outer iterations

<sup>4</sup> Extending (7b) to moist precipitating thermodynamics of [37] amounts to combining the moisture contribution, (58) in [37], to the density potential temperature in the buoyancy force with  $\hat{\theta}'$  in the  $V$  and  $W$  expressions (44) of the Appendix C.

in REF and GBIS semi-implicit integrators. Figure 5 shows the hemispheric patterns of the 18 day GBIS-REF departures of  $\theta'$  solutions on the O180 grid with left and right panels corresponding to the default and two outer iterations. Both results evince perfect equatorial symmetry with the GBIS and REF results differing pattern-wise in fine details everywhere but in the region where the wavetrain leading and trailing edges collapse evincing solution departures comparable to the solution amplitude at  $\sim 50\%$ . Moreover, the solutions departures are visibly smaller for the runs with two outer iterations. Although this illustrates the iteration convergence, it does not resolve which solver is more accurate. On the other hand, Fig. 6 quantifies the impact of the additional iteration on each solver, by showing differences of REF (left) and GBIS (right) results with two and one (default) outer iterations. Clearly the additional iteration has visibly smaller impact on the GBIS result, which documents that it is REF that approaches GBIS in Fig. 5, and not vice versa. Incidentally, the latter makes the GBIS run effectively cheaper than REF for short and medium-range applications, because adding the outer iteration to REF with effectively similar solution errors increases its execution time (otherwise comparable in both cases) by  $\sim 10\%$ .

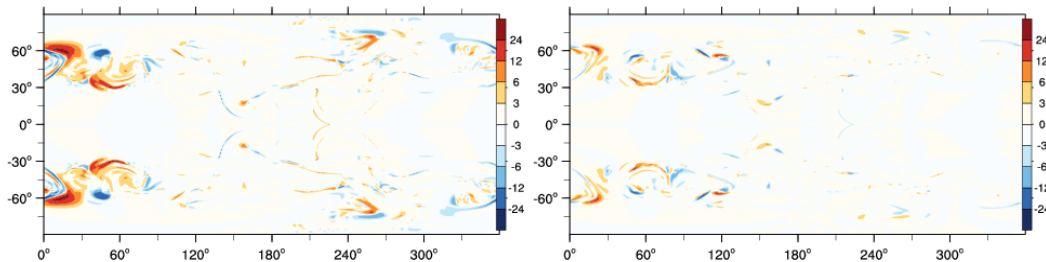


Fig. 6. The respective departures of REF (left) and GBIS (right) solutions with two and one (default) outer iterations.

## 5 CONCLUDING REMARKS

The key achievement of the technical development summarised in this paper is a novel numerical approach and implementation of perturbation equations for more accurate simulations of all scale atmospheric dynamics. The new perturbation form (7) of the compressible Euler equations and the associated numerical solvers extend the equivalent apparatus advanced in [35,15,16,36,37] for the equations formulated in terms of the pressure and entropy perturbations onto the velocity perturbations. This opens new opportunities for extended-range and seasonal weather and climate applications, by enabling exploitation as well as a dissection of the solution sensitivities to various processes and realisations of numerical errors.

Apart from the practical consequences of reducing grid imprinting on more

flexible but non-uniform meshes, the new formulation requires a learning effort in real applications in order to be used beneficially. The perturbation equations are formulated about a principally arbitrary ambient state that satisfies the generic equations (from which the perturbation forms derive) or a subset. Not all the ambient states are expected to be useful, and a separate research effort is required to identify suitable ambient states for weather simulations with full complexity. The examples provided in this paper assumed a class of idealised zonally uniform ambient states in a geostrophic balance (31). Such simple states already expose the complexity of the development, mainly concentrated in the coefficients of the elliptic BVP (27) at the heart of the large-time-step semi-implicit integrators (16) for the all-scale compressible Euler equations.

The tailored derivations of the BVP coefficients summarised in Appendices B and C are instructional, as they shed light on the physical significance of the new development and the associated interpretation of the governing equations. For instance, (39) reveals how the ambient shears modify the Coriolis force, hinting that the trapezoidal integrals of the  $-\mathbf{v}' \cdot \nabla \mathbf{u}_a$  terms on the rhs of the momentum (vector) equation (7b) should benefit long-term simulations of large scale flows dominated by vorticity dynamics. In the established formulation (11) the same terms are included in the advection, thus being subject to truncation terms that serve monotonicity of the transport but dilute the amplitude of the ambient balance, which is circumvented in (7b).

Extended-range simulations of the planetary baroclinic instability illustrate the impact of the new perturbation formulation. As all considered formulations are mathematically equivalent, and their associated solvers are formally second-order-accurate, we verified no significant differences in short- and medium-range weather evolution. The simulations show that extreme solution differences between different formulations are within 1% and 10% of the solution amplitude, respectively, after 10 and 15 days of the instability evolution, but become comparable to the amplitude (50%) three days later. At this later time there is a marked signal that (7b) offers improved accuracy in the long planetary waves, attributable to a better conditioning of the BVP problem. Because the accurate representation of the large scales is a prerequisite for extended-range predictability, the generalised perturbation equations offer significant potential for further evaluation.

The hypothesis that GBIS is also more accurate than REF due to an improved accuracy of the implicit-shear solutions in planetary scales is corroborated with similar EULAG simulations that integrate (11) on a regular longitude-latitude grid, using two variants of the operator preconditioning in the elliptic solver. The standard deflation preconditioner, common to EULAG and FVM, relies on the direct inversion in the vertical, whereas its optional (in EULAG) ADI extension [21] directly inverts the operator also in the zonal direction. Calculations with the ADI variant evince substantially smaller residual errors

on planetary scales (not shown).

All considerations so far exploited a pristine approach with perturbations defined with respect to the actual solutions of the generic equations. However, the developed numerical apparatus offers technical advantages equally applicable to approximate ambient states constructed based on alternative or surrogate models and/or (machine-learned) data. This may call for the inclusion of additional forcing terms (bias correction) to model the ambient state errors as opposed to bias correcting the entire state evolution—in the spirit of turbulence closures or continuous data assimilation [3]. However, importantly this will not affect the machinery of the semi-implicit integrators and the BVP coefficients. Consequently, the proposed solvers form the basis for the development of new multilevel methods, time parallel and/or hardware-failure resilient algorithms as well as blending with novel data-informed approaches.

*Acknowledgements:* This work was supported in part by funding received from the European Research Council under the European Union’s Seventh Framework Programme (FP7/2012/ERC Grant agreement no. 320375).

## Appendix A. Specifications of the spherical frame

In the spherical curvilinear framework of [22], the vector  $\mathbf{u}$  represents the physical velocity with components aligned at every point of the spherical shell with axes of a local Cartesian frame (subsequently marked as  $_c$ ) tangent to the lower surface ( $r = a$ ) of the shell;  $r$  is the radial component of the vector radius, and  $a$  is the radius of the sphere, cf. Fig. 7.7, section 7.2 in [7]. Consequently,  $dx_c = r \cos \phi d\lambda$ ,  $dy_c = r d\phi$  and  $z_c = r - a$ ; where  $\lambda$  and  $\phi$  denote longitude and latitude angles, respectively. Then, in the formalism of Sections 2 and 3 and in the absence of coordinate stretching,  $x = a\lambda$ ,  $y = a\phi$ , and  $z = z_c$ ; thereby effectively employing longitude-latitude coordinates standard in many global atmospheric models [38]. Furthermore, the coefficient matrix  $\widetilde{\mathbf{G}}$  consists of zero off-diagonal entries, whereas  $\widetilde{G}_1^1 = [\Gamma \cos(y/a)]^{-1}$ ,  $\widetilde{G}_2^2 = \Gamma^{-1}$ , and  $\widetilde{G}_3^3 = 1$ . Here,  $\Gamma = 1 + \chi z/a$ , and indices 1, 2, and 3 correspond to  $x$ ,  $y$ , and  $z$  components. Consequently, the Jacobian is  $\mathcal{G} = \Gamma^2 \cos(y/a)$ . The parameter  $\chi$  is set to unity by default; whereas the optional setting  $\chi = 0$  selects the shallow atmosphere approximation in the governing PDEs [44].

In the momentum equation, the components of the Coriolis acceleration are

$$\begin{aligned}
-\mathbf{f} \times \mathbf{u} = & \left[ v f_0 \sin(y/a) - \chi w f_0 \cos(y/a), \right. \\
& -u f_0 \sin(y/a), \\
& \left. \chi u f_0 \cos(y/a) \right], \tag{32}
\end{aligned}$$

where  $\mathbf{u} = [u, v, w]$  and  $f_0 = 2|\boldsymbol{\Omega}|$ . Furthermore, the metric forcings (viz., component-wise Christoffel terms associated with the convective derivative of the physical velocity) are,

$$\begin{aligned}
\mathcal{M}(\mathbf{u}) = (\Gamma a)^{-1} & \left[ \tan(y/a) u v - \chi u w, \right. \\
& -\tan(y/a) u u - \chi v w, \\
& \left. \chi (u u + v v) \right]. \tag{33}
\end{aligned}$$

## Appendix B. Details of the linear operator on the lhs of (23a)

Expanding (21) in components leads to

$$\begin{aligned}
u'^x + \tau^u & \left( u'^x \widetilde{\partial}_x u_a^x + u'^y \widetilde{\partial}_y u_a^x + u'^z \widetilde{\partial}_z u_a^x \right) + \tau^u \left( -u'^y f^z + u'^z f^y \right) \\
& - \tau^u \tau^\theta \left( u'^x \widetilde{\partial}_x \Theta_a + u'^y \widetilde{\partial}_y \Theta_a + u'^z \widetilde{\partial}_z \Theta_a \right) \widetilde{\partial}_x \phi_a = \widehat{u'^x} - \tau^u \Theta^* \widetilde{\partial}_x \phi', \tag{34a}
\end{aligned}$$

$$\begin{aligned}
u'^y + \tau^u & \left( u'^x \widetilde{\partial}_x u_a^y + u'^y \widetilde{\partial}_y u_a^y + u'^z \widetilde{\partial}_z u_a^y \right) + \tau^u \left( -u'^z f^x + u'^x f^z \right) \\
& - \tau^u \tau^\theta \left( u'^x \widetilde{\partial}_x \Theta_a + u'^y \widetilde{\partial}_y \Theta_a + u'^z \widetilde{\partial}_z \Theta_a \right) \widetilde{\partial}_y \phi_a = \widehat{u'^y} - \tau^u \Theta^* \widetilde{\partial}_y \phi', \tag{34b}
\end{aligned}$$

$$\begin{aligned}
u'^z + \tau^u & \left( u'^x \widetilde{\partial}_x u_a^z + u'^y \widetilde{\partial}_y u_a^z + u'^z \widetilde{\partial}_z u_a^z \right) + \tau^u \left( -u'^x f^y + u'^y f^x \right) \\
& - \tau^u \tau^\theta \left( u'^x \widetilde{\partial}_x \Theta_a + u'^y \widetilde{\partial}_y \Theta_a + u'^z \widetilde{\partial}_z \Theta_a \right) \widetilde{\partial}_z \phi_a = \widehat{u'^z} - \tau^u \Theta^* \widetilde{\partial}_z \phi', \tag{34c}
\end{aligned}$$

which upon regrouping all terms in the spirit of a matrix-vector product,

$$\begin{aligned}
& u'^x [1 + \tau^u (\widetilde{\partial}_x u_a^x - \tau^\theta \widetilde{\partial}_x \Theta_a \widetilde{\partial}_x \phi_a)] \\
& + u'^y [\tau^u (\widetilde{\partial}_y u_a^x - \tau^\theta \widetilde{\partial}_y \Theta_a \widetilde{\partial}_x \phi_a - f^z)] \\
& + u'^z [\tau^u (\widetilde{\partial}_z u_a^x - \tau^\theta \widetilde{\partial}_z \Theta_a \widetilde{\partial}_x \phi_a + f^y)] = \widehat{u'^x} - \tau^u \Theta^* \widetilde{\partial}_x \phi', \tag{35a}
\end{aligned}$$

$$\begin{aligned}
& u'^x [\tau^u (\widetilde{\partial}_x u_a^y - \tau^\theta \widetilde{\partial}_x \Theta_a \widetilde{\partial}_y \phi_a + f^z)] \\
& + u'^y [1 + \tau^u (\widetilde{\partial}_y u_a^y - \tau^\theta \widetilde{\partial}_y \Theta_a \widetilde{\partial}_y \phi_a)] \\
& + u'^z [\tau^u (\widetilde{\partial}_z u_a^y - \tau^\theta \widetilde{\partial}_z \Theta_a \widetilde{\partial}_y \phi_a - f^x)] = \widehat{u'^y} - \tau^u \Theta^* \widetilde{\partial}_y \phi', \tag{35b}
\end{aligned}$$

$$\begin{aligned}
& u'^x [\tau^u (\widetilde{\partial}_x u_a^z - \tau^\theta \widetilde{\partial}_x \Theta_a \widetilde{\partial}_z \phi_a - f^y)] \\
& + u'^y [\tau^u (\widetilde{\partial}_y u_a^z - \tau^\theta \widetilde{\partial}_y \Theta_a \widetilde{\partial}_z \phi_a + f^x)] \\
& + u'^z [1 + \tau^u (\widetilde{\partial}_z u_a^z - \tau^\theta \widetilde{\partial}_z \Theta_a \widetilde{\partial}_z \phi_a)] = \widehat{u'^z} - \tau^u \Theta^* \widetilde{\partial}_z \phi', \tag{35c}
\end{aligned}$$

reveals the entries of the linear operator  $\mathbf{L} = [l_{ij}]$  in (23a) as

$$\begin{aligned} l_{11} &= 1 + \tau^u (\widetilde{\partial}_x u_a^x - \tau^\theta \widetilde{\partial}_x \Theta_a \widetilde{\partial}_x \phi_a) , \\ l_{12} &= \tau^u (\widetilde{\partial}_y u_a^x - \tau^\theta \widetilde{\partial}_y \Theta_a \widetilde{\partial}_x \phi_a - f^z) , \\ l_{13} &= \tau^u (\widetilde{\partial}_z u_a^x - \tau^\theta \widetilde{\partial}_z \Theta_a \widetilde{\partial}_x \phi_a + f^y) , \end{aligned} \quad (36a)$$

$$\begin{aligned} l_{21} &= \tau^u (\widetilde{\partial}_x u_a^y - \tau^\theta \widetilde{\partial}_x \Theta_a \widetilde{\partial}_y \phi_a + f^z) , \\ l_{22} &= 1 + \tau^u (\widetilde{\partial}_y u_a^y - \tau^\theta \widetilde{\partial}_y \Theta_a \widetilde{\partial}_y \phi_a) , \\ l_{23} &= \tau^u (\widetilde{\partial}_z u_a^y - \tau^\theta \widetilde{\partial}_z \Theta_a \widetilde{\partial}_y \phi_a - f^x) , \end{aligned} \quad (36b)$$

$$\begin{aligned} l_{31} &= \tau^u (\widetilde{\partial}_x u_a^z - \tau^\theta \widetilde{\partial}_x \Theta_a \widetilde{\partial}_z \phi_a - f^y) , \\ l_{32} &= \tau^u (\widetilde{\partial}_y u_a^z - \tau^\theta \widetilde{\partial}_y \Theta_a \widetilde{\partial}_z \phi_a) + f^x , \\ l_{33} &= 1 + \tau^u (\widetilde{\partial}_z u_a^z - \tau^\theta \widetilde{\partial}_z \Theta_a \widetilde{\partial}_z \phi_a) . \end{aligned} \quad (36c)$$

Having defined all entries of  $\mathbf{L}$ , its inverse is evaluated as analytically as  $\mathbf{L}^{-1} = \{\mathbf{L}\}^{-1} \text{adj}(\mathbf{L})$  where  $\{\mathbf{L}\} \equiv \det(\mathbf{L})$  and ‘‘adj’’ denotes the matrix adjugate, with column-wise entries:

$$\begin{aligned} \text{adj}l_{11} &= l_{22}l_{33} - l_{23}l_{32} , \\ \text{adj}l_{21} &= l_{23}l_{31} - l_{21}l_{33} , \\ \text{adj}l_{31} &= l_{21}l_{33} - l_{23}l_{31} , \end{aligned} \quad (37a)$$

$$\begin{aligned} \text{adj}l_{12} &= l_{13}l_{32} - l_{12}l_{33} , \\ \text{adj}l_{22} &= l_{11}l_{33} - l_{13}l_{31} , \\ \text{adj}l_{32} &= l_{12}l_{31} - l_{11}l_{32} , \end{aligned} \quad (37b)$$

$$\begin{aligned} \text{adj}l_{13} &= l_{12}l_{23} - l_{13}l_{22} , \\ \text{adj}l_{23} &= l_{13}l_{21} - l_{11}l_{23} , \\ \text{adj}l_{33} &= l_{11}l_{22} - l_{12}l_{21} . \end{aligned} \quad (37c)$$

## Appendix C. Further details of the Poisson problem (28)

To highlight the connection of the matrix-algebra formalism of Appendix B with hand-derived compact formulae of [22], it is instructive to specify further details of (28), for the perturbation equations (7) and a class of zonally-uniform ambient states (31) assumed in Sections 3.2.2 and 4. In particular, when solving (7b), accounting for  $\vartheta_x \equiv 0$  and adopting normalisations accordant with [22] (to be explained shortly),

$$\begin{aligned} \mathcal{E}^{-1} &= [\mathcal{G}_3 \widetilde{\mathcal{F}}_2 \widetilde{\mathcal{F}}_3 + \mathcal{G}_2 (1 + \widetilde{\mathcal{F}}_2 \widetilde{\mathcal{F}}_2)] \vartheta_y + [\mathcal{G}_2 \widetilde{\mathcal{F}}_2 \widetilde{\mathcal{F}}_3 + \mathcal{G}_3 (1 + \widetilde{\mathcal{F}}_3 \widetilde{\mathcal{F}}_3)] \vartheta_z \\ &\quad + (1 + \widetilde{\alpha}^*) (1 + \widetilde{\mathcal{F}}_2 \widetilde{\mathcal{F}}_2 + \widetilde{\mathcal{F}}_3 \widetilde{\mathcal{F}}_3) . \end{aligned} \quad (38)$$

Here  $\mathcal{G}_2$  and  $\mathcal{G}_3$  correspond to normalised meridional and radial components of  $\theta_0^{-1}\widetilde{\mathbf{G}}\nabla\phi_a$ , and

$$\widetilde{\mathcal{F}}_2 = \mathcal{F}_2 + \widetilde{\partial}_z^* u_a, \quad \widetilde{\mathcal{F}}_3 = \mathcal{F}_3 - \widetilde{\partial}_y^* u_a, \quad (39)$$

where the symbols  $\mathcal{F}_j$ ,  $\vartheta_\zeta$ ,  $\widetilde{\alpha}^*$  correspond to normalised components of the Coriolis parameter, components of the ambient gradients  $\widetilde{\nabla}\Theta_a$  and  $\alpha^\theta$ , and the asterisk by  $\widetilde{\partial}_y$ ,  $\widetilde{\partial}_z$  marks the normalisation.

The functions  $\mathcal{V}^p$  and  $\mathcal{C}^{pk}$  from the rhs of (29) are compactly written as

$$\begin{aligned} \mathcal{V}^1 &= \mathcal{A}U + \mathcal{B}V - \mathcal{X}W, \\ \mathcal{V}^2 &= \mathcal{C}U + \mathcal{D}V + \mathcal{Y}W, \\ \mathcal{V}^3 &= \mathcal{H}U + \mathcal{I}V + \mathcal{Z}W. \end{aligned} \quad (40)$$

where the coefficients  $\mathcal{A}$  to  $\mathcal{I}$  (named after [22]) and  $\mathcal{X}$  to  $\mathcal{Z}$  (introduced here for conciseness) are equal to

$$\begin{aligned} \mathcal{A} &= \mathcal{R} + \mathcal{G}_2\vartheta_y + \mathcal{G}_3\vartheta_z, \\ \mathcal{B} &= \mathcal{R}\widetilde{\mathcal{F}}_3 + \mathcal{G}_3(\widetilde{\mathcal{F}}_2\vartheta_y + \widetilde{\mathcal{F}}_3\vartheta_z), \\ \mathcal{X} &= -\mathcal{R}\widetilde{\mathcal{F}}_2 - \mathcal{G}_2(\widetilde{\mathcal{F}}_2\vartheta_y + \widetilde{\mathcal{F}}_3\vartheta_z), \end{aligned} \quad (41)$$

$$\begin{aligned} \mathcal{C} &= -\mathcal{R}\mathcal{F}_3 - (\mathcal{G}_2\mathcal{F}_2 + \mathcal{G}_3\mathcal{F}_3)\vartheta_z, \\ \mathcal{D} &= \mathcal{R}(1 + \mathcal{F}_2\widetilde{\mathcal{F}}_2) + \mathcal{G}_3\vartheta_z, \\ \mathcal{Y} &= \mathcal{R}\widetilde{\mathcal{F}}_2\mathcal{F}_3 - \mathcal{G}_2\vartheta_z, \end{aligned} \quad (42)$$

and

$$\begin{aligned} \mathcal{H} &= \mathcal{R}\mathcal{F}_2 + (\mathcal{G}_2\mathcal{F}_2 + \mathcal{G}_3\mathcal{F}_3)\vartheta_y, \\ \mathcal{I} &= \mathcal{R}\mathcal{F}_2\widetilde{\mathcal{F}}_3 - \mathcal{G}_3\vartheta_y, \\ \mathcal{Z} &= \mathcal{R}(1 + \mathcal{F}_3\widetilde{\mathcal{F}}_3) + \mathcal{G}_2\vartheta_y \end{aligned} \quad (43)$$

Here as well as in (38) and the model code,  $\mathcal{R} = \tau^u/\tau^\theta$  (recall Eqs. 19), whereas all the components of the Coriolis parameter, ambient gradients  $\widetilde{\nabla}\Theta_a$  and generalised buoyancy  $\theta_0^{-1}\widetilde{\mathbf{G}}\nabla\phi_a$  are multiplied by  $\tau^u$ , in effect of which the factor  $(1 + \alpha^*)^{-1} \equiv \tau^u\delta_h^{-1}t$  in the corresponding formulae of [22] is absorbed in definitions of the normalised fields. Furthermore, the velocities  $U$ ,  $V$  and  $W$  are

$$\begin{aligned} U &= \beta\widehat{u} + u_a, \\ V &= \beta\widehat{v} + \widetilde{\mathcal{G}}_2\widehat{\theta}' + \delta_h t f_3 u_a, \\ W &= \beta\widehat{w} + \widetilde{\mathcal{G}}_3\widehat{\theta}' - \delta_h t f_2 u_a, \end{aligned} \quad (44)$$

where  $\beta = \delta_h t/\tau^u$  is the reciprocal of the normalising prefactor in (22),<sup>5</sup> and  $\widetilde{\mathcal{G}}_k = \mathcal{G}_k/\mathcal{R}$ .

<sup>5</sup> Note two typos in (A.16) of [22]:  $\widetilde{\theta}'$  should be  $LE(\widetilde{\theta}')$  and  $\theta' = \theta - \theta_e$ , for consis-

The coefficients  $\mathcal{C}^{pk}$  used in (29) take the explicit form:

$$\begin{aligned}
\mathcal{C}^{11} &= \mathcal{R}(\tilde{G}_1^1 + \tilde{G}_2^1 \tilde{\mathcal{F}}_3) + \mathcal{G}_2 \tilde{G}_1^1 \vartheta_y + \mathcal{G}_3 \left[ \tilde{G}_2^1 \tilde{\mathcal{F}}_2 \vartheta_y + (\tilde{G}_1^1 + \tilde{G}_2^1 \tilde{\mathcal{F}}_3) \vartheta_z \right], \\
\mathcal{C}^{12} &= \mathcal{R}(\tilde{G}_1^2 + \tilde{G}_2^2 \tilde{\mathcal{F}}_3) + \mathcal{G}_2 \tilde{G}_1^2 \vartheta_y + \mathcal{G}_3 \left[ \tilde{G}_2^2 \tilde{\mathcal{F}}_2 \vartheta_y + (\tilde{G}_1^2 + \tilde{G}_2^2 \tilde{\mathcal{F}}_3) \vartheta_z \right], \\
\mathcal{C}^{13} &= \mathcal{R}(\tilde{G}_1^3 + \tilde{G}_2^3 \tilde{\mathcal{F}}_3 - \tilde{G}_3^3 \tilde{\mathcal{F}}_2) + \mathcal{G}_3 \left[ \tilde{G}_2^3 \tilde{\mathcal{F}}_2 \vartheta_y + (\tilde{G}_1^3 + \tilde{G}_2^3 \tilde{\mathcal{F}}_3) \vartheta_z \right] \\
&\quad + \mathcal{G}_y \left[ -\tilde{G}_3^3 \tilde{\mathcal{F}}_3 \vartheta_z + (\tilde{G}_1^3 - \tilde{G}_3^3 \tilde{\mathcal{F}}_2) \vartheta_y \right],
\end{aligned} \tag{45}$$

$$\begin{aligned}
\mathcal{C}^{21} &= \mathcal{R} \left[ -\tilde{G}_1^1 \tilde{\mathcal{F}}_3 + \tilde{G}_2^1 (1 + \tilde{\mathcal{F}}_2 \tilde{\mathcal{F}}_2) \right] - \left[ \mathcal{G}_2 \tilde{G}_1^1 \tilde{\mathcal{F}}_2 - \mathcal{G}_3 (\tilde{G}_2^1 - \tilde{G}_1^1 \tilde{\mathcal{F}}_3) \right] \vartheta_z, \\
\mathcal{C}^{22} &= \mathcal{R} \left[ -\tilde{G}_1^2 \tilde{\mathcal{F}}_3 + \tilde{G}_2^2 (1 + \tilde{\mathcal{F}}_2 \tilde{\mathcal{F}}_2) \right] - \left[ \mathcal{G}_2 \tilde{G}_1^2 \tilde{\mathcal{F}}_2 - \mathcal{G}_3 (\tilde{G}_2^2 - \tilde{G}_1^2 \tilde{\mathcal{F}}_3) \right] \vartheta_z, \\
\mathcal{C}^{23} &= \mathcal{R} \left[ -\tilde{G}_1^3 \tilde{\mathcal{F}}_3 + \tilde{G}_2^3 (1 + \tilde{\mathcal{F}}_2 \tilde{\mathcal{F}}_2) + \tilde{G}_3^3 \tilde{\mathcal{F}}_2 \tilde{\mathcal{F}}_3 \right] \\
&\quad + \left[ \mathcal{G}_3 (\tilde{G}_2^3 - \tilde{G}_1^3 \tilde{\mathcal{F}}_3) - \mathcal{G}_2 (\tilde{G}_3^3 + \tilde{G}_1^3 \tilde{\mathcal{F}}_2) \right] \vartheta_z,
\end{aligned} \tag{46}$$

$$\begin{aligned}
\mathcal{C}^{31} &= \mathcal{R}(\tilde{G}_1^1 \tilde{\mathcal{F}}_2 + \tilde{G}_2^1 \tilde{\mathcal{F}}_2 \tilde{\mathcal{F}}_3) + \left[ \mathcal{G}_2 \tilde{G}_1^1 \tilde{\mathcal{F}}_2 + \mathcal{G}_3 (\tilde{G}_1^1 \tilde{\mathcal{F}}_3 - \tilde{G}_2^1) \right] \vartheta_y, \\
\mathcal{C}^{32} &= \mathcal{R}(\tilde{G}_1^2 \tilde{\mathcal{F}}_2 + \tilde{G}_2^2 \tilde{\mathcal{F}}_2 \tilde{\mathcal{F}}_3) + \left[ \mathcal{G}_2 \tilde{G}_1^2 \tilde{\mathcal{F}}_2 + \mathcal{G}_3 (\tilde{G}_1^2 \tilde{\mathcal{F}}_3 - \tilde{G}_2^2) \right] \vartheta_y, \\
\mathcal{C}^{33} &= \mathcal{R} \left[ \tilde{G}_1^3 \tilde{\mathcal{F}}_2 + \tilde{G}_2^3 \tilde{\mathcal{F}}_2 \tilde{\mathcal{F}}_3 + \tilde{G}_3^3 (1 + \tilde{\mathcal{F}}_2 \tilde{\mathcal{F}}_3) \right] \\
&\quad + \left[ \mathcal{G}_2 (\tilde{G}_1^3 \tilde{\mathcal{F}}_2 + \tilde{G}_3^3) + \mathcal{G}_3 (\tilde{G}_1^3 \tilde{\mathcal{F}}_3 - \tilde{G}_2^3) \vartheta_y \right].
\end{aligned} \tag{47}$$

The provided expressions are general, in that they account for all the four forms of the considered perturbation equations. Namely, for (10)

$$\mathcal{G}_2 \equiv 0, \quad \mathcal{G}_3 \equiv \mathcal{G}, \tag{48}$$

where  $\mathcal{G}$  is the normalised gravitational acceleration of [22]; whereas for (12)

$$\tilde{\mathcal{F}}_2 \equiv \tilde{\mathcal{F}}_2, \quad \tilde{\mathcal{F}}_3 \equiv \tilde{\mathcal{F}}_3. \tag{49}$$

Furthermore, (11) combines (48) and (49), reproducing the formulae of [22]—all under the assumption of  $\vartheta_x \equiv 0$ . Consequently, the compact modifications (48) and (49) verify the field  $\mathcal{E}$  specified in (A.4) of [22], the explicit  $\mathcal{V}^p = \check{\mathbf{u}}^p / \mathcal{E}$  velocities in their formulae (A.5)-(A.7) as well as the coefficients  $\mathcal{A}$ - $\mathcal{I}$  in their (A.8)-(A.15). The latter coefficients correspond to the entries of the  $\mathbf{L}^{-1} \mathcal{E}^{-1}$  operator that (here) acts on the explicit counterpart of the physical velocity  $\widehat{\mathbf{u}}^i + \mathbf{L} \mathbf{u}_a$ —the components of which correspond in turn to  $U$ ,  $V$  and  $W$  converted to  $\mathcal{V}^p|_{p=1,2,3}$  in (A.5)-(A.7) of [22] and specified in their (A.14)-(A.16). Furthermore, these modifications also verify the  $\mathcal{C}^{pk}$  coefficients in (A.17)-(A.25).

---

tency with their Eq. (12).

## References

- [1] I. Barstad, W.W. Grabowski, P.K. Smolarkiewicz, Characteristics of large-scale orographic precipitation: Evaluation of linear model in idealized problems, *J. Hydrol.* 340 (2007) 78-90.
- [2] P. Bauer, A. Thorpe, G. Brunet, The quiet revolution of numerical weather prediction, *Nature* 525 (2015) 47–55.
- [3] J.-F. Cossette, P. Charbonneau, P.K. Smolarkiewicz, M.P. Rast, Magnetically-modulated heat transport in a global simulation of solar magneto-convection, *Astrophysics. J.* 841 (2017) 65 (17pp).
- [4] A. Dörnbrack, J.D. Doyle, T.P. Lane, R.D. Sharman, P.K. Smolarkiewicz, On physical realizability and uncertainty of numerical solutions, *Atmos. Sci. Lett.* 6 (2005) 118-122. doi:10.1002/asl.100
- [5] D.R. Durran, J.B. Klemp, A compressible model for the simulation of moist mountain waves, *Mon. Weather Rev.* 111 (1983) 2341–2361.
- [6] D.R. Durran, Improving the anelastic approximation. *J. Atmos. Sci.* 46 (1989) 1453–1461.
- [7] J.A. Dutton, *The Ceaseless Wind*, Dover Publications (1986) pp. 617.
- [8] M. Ghizaru, P. Charbonneau, P.K. Smolarkiewicz, Magnetic Cycles in Global Large-eddy Simulations of Solar Convection, *Astrophys. J. Lett.* 715 (2010) L133–L137
- [9] <https://hiwpp.noaa.gov/>.
- [10] C. Jablonowski, D.L. Williamson, A baroclinic instability test case for atmospheric model dynamical cores, *Q.J.R. Meteorol. Soc.* 132 (2006) 2943–2975.
- [11] C. Kühnlein, P.K. Smolarkiewicz, A. Dörnbrack, Modelling atmospheric flows with adaptive moving meshes, *J. Comput. Phys.* 231 (2012) 2741–2763.
- [12] C. Kühnlein, C. Keil, G.C. Craig, C. Gebhardt, The impact of downscaled initial condition perturbations on convective-scale ensemble forecasts of precipitation, *Q. J. Roy. Meteorol. Soc.*, 140 (2014) 1552–1562.
- [13] C. Kühnlein, P.K. Smolarkiewicz, An unstructured-mesh finite-volume MPDATA for compressible atmospheric dynamics, *J. Comput. Phys.* 334 (2017), 16–30.
- [14] C. Kühnlein, S. Malardel, P.K. Smolarkiewicz, Simulation in the greyzone with the Finite-Volume Module of the IFS, Workshop: Shedding light on the greyzone, ECMWF, Reading, 13-16 Nov. 2017; <https://www.ecmwf.int/sites/default/files/elibrary/2017/17804-simulation-greyzone-finite-volume-module-ifs.pdf>

- [15] M.J. Kurowski, W.W. Grabowski, and P.K. Smolarkiewicz, Anelastic and compressible simulations of moist deep convection, *J. Atmos. Sci.* 71 (2014) 3767–3787.
- [16] M.J. Kurowski, W.W. Grabowski, and P.K. Smolarkiewicz, Anelastic and compressible simulations of moist dynamics at planetary scales, *J. Atmos. Sci.* 72 (2015) 3975–3995.
- [17] M. Leutbecher et al., Stochastic representations of model uncertainties at ECMWF: state of the art and future vision, *Q.J. Roy. Meteorol. Soc.*, 143 (2017) 2315–2339.
- [18] F.B. Lipps, R.S. Hemler, A scale analysis of deep moist convection and some related numerical calculations, *J. Atmos. Sci.* 39 (1982) 2192–2210.
- [19] H.R., Miller, 1991: A horror story about integration methods, *J. Comput. Phys.*, 93 (1991) 469–476.
- [20] L. Magnusson, M. Alonso-Balmaseda, S. Corti, F. Molteni, T. Stockdale, Evaluation of forecast strategies for seasonal and decadal forecasts in presence of systematic model errors, *Clim. Dyn.* (2013), 41:23932409.
- [21] Z.P. Piotrowski, B. Matejczyk, L. Marcinkowski, P.K. Smolarkiewicz, Parallel ADI preconditioners for all-scale atmospheric models, in *Parallel Processing and Applied Mathematics*, LNCS 9574, Springer International Publishing, 607-618.
- [22] J.M. Prusa, P.K. Smolarkiewicz, An all-scale anelastic model for geophysical flows: dynamic grid deformation, *J. Comput. Phys.* 190 (2003) 601–622.
- [23] J.M. Prusa, P.K. Smolarkiewicz, A.A Wyszogrodzki, EULAG, a computational model for multiscale flows, *Comput. Fluids* 37 (2008) 1193–1207
- [24] E. Racine, P. Charbonneau, M. Ghizaru, A. Bouchat, P.K. Smolarkiewicz, On the mode of dynamo action in a global large-eddy simulation of solar convection, *Astrophys. J.* 735:46 (2011) 22 pp.
- [25] P.K. Smolarkiewicz, L.G. Margolin, Variational solver for elliptic problems in atmospheric flows, *Appl. Math. Comp. Sci.* 4 (1994) 527–551.
- [26] P.K. Smolarkiewicz, L.G. Margolin, A.A Wyszogrodzki, A class of nonhydrostatic global models, *J. Atmos. Sci.* 58 (2001) 349–364.
- [27] P.K. Smolarkiewicz, L.G. Margolin: On forward-in-time differencing for fluids: an Eulerian/semi-Lagrangian non-hydrostatic model for stratified flows, *Atmos.-Ocean*, 35 (1997) 127–152.
- [28] P.K. Smolarkiewicz, J.A. Prusa, Towards mesh adaptivity for geophysical turbulence: continuous mapping approach, *Int. J. Numer. Meth. Fluids* 47 (2005) 789–801.
- [29] P.K. Smolarkiewicz, J. Szmelter, MPDATA: An edge-based unstructured-grid formulation, *J. Comput. Phys.* 206 (2005) 624-649.

- [30] P.K. Smolarkiewicz, Multidimensional positive definite advection transport algorithm: an overview, *Int. J. Numer. Meth. Fluids* 50 (2006) 1123–1144.
- [31] P.K. Smolarkiewicz, R. Sharman, J. Weil, S.G. Perry, D. Heist, G. Bowker, Building resolving large-eddy simulations and comparison with wind tunnel experiments, *J. Comput. Phys.* 227 (2007) 633–653.
- [32] P.K. Smolarkiewicz, A. Dörnbrack, Conservative integrals of adiabatic Durran’s equations, *Int. J. Numer. Meth. Fluids* 56 (2008) 1513–1519. doi: 10.1002/fld.1601
- [33] P.K. Smolarkiewicz, J. Szmelter, A nonhydrostatic unstructured-mesh soundproof model for simulation of internal gravity waves, *Acta Geophysica* 59 (2011) 1109–1134.
- [34] P.K. Smolarkiewicz, P. Charbonneau, EULAG, a computational model for multiscale flows: An MHD extension, *J. Comput. Phys.* 236 (2013) 608–623.
- [35] P.K. Smolarkiewicz, C. Kühnlein, N.P. Wedi, A consistent framework for discrete integrations of soundproof and compressible PDEs of atmospheric dynamics, *J. Comput. Phys.* 263 (2014) 185–205
- [36] P.K. Smolarkiewicz, W. Deconinck, M. Hamrud, C. Kühnlein, G. Mozdzyński, J. Szmelter, N.P. Wedi, A finite-volume module for simulating global all-scale atmospheric flows, *J. Comput. Phys.* 315 (2016) 287–304.
- [37] P.K. Smolarkiewicz, C. Kühnlein, W.W. Grabowski, A finite-volume module for cloud-resolving simulations global atmospheric flows, *J. Comput. Phys.* 341 (2017) 208–229.
- [38] J. Szmelter, P.K. Smolarkiewicz, An edge-based unstructured mesh discretisation in geospherical framework, *J. Comput. Phys.* 229 (2010) 4980–4995.
- [39] A. Warn-Varnas, J. Hawkins, P.K. Smolarkiewicz, S.A. Chin-Bing, D. King, Z. Hallock, Solitary wave effects north of Strait of Messina, *Ocean Modelling* 18 (2007) 97–121.
- [40] P.A. Ullrich, T. Melvin, C. Jablonowski, A. Staniforth, A proposed baroclinic wave test case for deep- and shallow-atmosphere dynamical cores, *Q.J. Roy. Meteorol. Soc.*, 140 (2014) 1590–1602.
- [41] P.A. Ullrich, C. Jablonowski, K.A. Reed, C. Zarzycki, P.H. Lauritzen, R.D. Nair, J. Kent, A. Verlet-Banide, Dynamical core model intercomparison project (DCMIP2016) test case document, <https://github.com/ClimateGlobalChange/DCMIP2016>.
- [42] N.P. Wedi, P.K. Smolarkiewicz, Extending Gal-Chen and Somerville terrain-following coordinate transformation on time dependent curvilinear boundaries, *J. Comput. Phys.* 193 (2004) 1–20.
- [43] N.P. Wedi, P.K. Smolarkiewicz, Direct numerical simulation of the Plumb-McEwan laboratory analog of the QBO, *J. Atmos. Sci.* 63 (2006) 3326–3252.

- [44] N.P. Wedi, P.K. Smolarkiewicz, A framework for testing global nonhydrostatic models, *Q.J. Roy. Meteorol. Soc.*, 135 (2009) 469–484.
- [45] N.P. Wedi, P.K. Smolarkiewicz, A nonlinear perspective on the dynamics of the MJO: idealized large-eddy-simulations, *J. Atmos. Sci.* 67 (2010) 1202–1217.
- [46] N.P. Wedi, P. Bauer, W. Deconinck, M. Diamantakis, M. Hamrud, C. Kühnlein, S. Malardel, K. Mogensen, G. Mozdzyński, P.K. Smolarkiewicz, The modelling infrastructure of the Integrated Forecasting System: Recent advances and future challenges, Technical Memorandum 760 (2015), ECMWF, pp. 48.
- [47] F. Zhang, N. Bei, R. Rotunno, C. Snyder, Mesoscale predictability of moist baroclinic waves: convection-permitting experiments and multistage error growth dynamics, *J. Atmos. Sci.* 64 (2007) 3579–3594.